Poroelasticity contributes to hydraulic-stimulation induced pressure changes

N.O. Dutler[1,2], B. Valley[1,2], F. Amann[1,3], M. Jalali[1,3], L. Villiger[1,4], H. Krietsch[1,5], V. Gischig[1,6], J. Doetsch[1,4], D. Giardini[1,4]

[1]Swiss Competence Center for Energy Research – Supply of Electricity (SCCER-SoE), ETH Zurich, Switzerland

[2]Center for Hydrogeology and Geothermics, University of Neuchâtel, Switzerland

[3]Department of Engineering Geology and Hydrogeology, RWTH Aachen, Germany

[4]Department of Earth Science, ETH Zurich, Switzerland

[5]iLF Beratende Ingenieure AG, Zurich, Switzerland

[6]CSD Ingenieure AG, Bern, Switzerland

Corresponding author: Nathan Dutler (nathan.dutler@unine.ch)

Key Points:

- Pore pressure time series reveale a near-field response dominated by pressure diffusion
- The far-field is dominated by a quasi-instantaneous poro-elastic response due to the static anisotropic stress field
- Injection data showed pressure changes can extend 3–5 times farther than the pressurized volume because of poroelasticity

Abstract

High-pressure fluid injections cause transient pore pressure changes over large distances, which may induce seismicity. The zone of influence for such an injection was studied at high spatial resolutions in six decameter-scaled fluid injection experiments in crystalline rock. Pore pressure time series revealed two distinct responses based on the lag time and magnitude of pressure change, namely, a near- and far-field response. The near-field response is due to pressure diffusion. In the far-field, the fast response time and decay of pressure changes are produced by effective stress changes in the anisotropic stress field. Our experiments prove for the first time that fracture fluid pressure perturbations around the injection point are not limited to the near-field and can extend beyond the pressurized zone.

Plain Language Summary

The far-field pore pressure response in geological reservoirs due to high pressure fluid injection is not clarified yet. Direct observations of far-field pore pressure changes were analysed in the framework of the In-Situ Stimulation and Circulation project executed at the Grimsel Test Site. The findings show two distinct behaviour, one related to pore pressure diffusion in the near-field of the injection and another one related to poro-elastic effects.

1 Introduction

[1] Hydraulic stimulation operations for enhanced geothermal systems (EGSs), petroleum applications, and wastewater disposal wells are potential sources of seismic hazards. In many places, the high-pressure and/or massive volume of injections has led to an increase in the frequency and magnitude of earthquakes (Bao & Eaton, 2016; Ellsworth, 2013; Frohlich, 2012). Presently, predictions of seismic hazards from injections remain difficult, and determinations of the causality of earthquakes located at a large distance (> 10 km) from injection locations are particularly arduous (Goebel et al., 2017; Keranen et al. 2014).

[2] The possible underpinning mechanisms remain under debate. Injection-induced seismicity is frequently explained by the pore pressure increase within the rock mass connected with the injection well. This zone can be referred to as the ‘pressurized zone’, and it can be illuminated by active seismic measurements during high-pressure fluid injections (Calò et al., 2011; Doetsch et al., 2018a; Schopper et al. 2020), as the relative change in p-wave velocity is directly linked to pore pressure changes. These pore pressure changes can lead to fault ruptures, and if the energy at the fracture tip overcomes the tensile strength of the rock, new fractures can be created.

[3] Within the pressurized zone, in the near-field of the injection site, the pore pressure distribution is dominated by fluid flow along a pressure gradient, i.e., pressure diffusion. However, the time scale for diffusion-induced pore pressure changes is too slow to explain rapid far-field pressure changes and remotely induced seismic events. One hypothesis explaining remote seismicity is that such activity might be associated with aseismic slip processes. Aseismic slip has been observed in-situ in response to fluid injection (Guglielmi et al., 2015) and can potentially extend beyond the pressurized zone (Bhaattacharya & Cappa, 2015). An alternative hypothesis involves poroelastic processes, which can be used to explain pressure changes caused by rock deformation and associated pore space variations reaching beyond the pressurized zone. This hypothesis has been invoked to describe earthquakes induced more than 30 km away from the injection point (Goebel & Brodsky, 2018).

[4] Water level variations in wells related to earthquakes also can be explained by poroelastic effects, and these events offer insights into hydromechanical coupled processes in the crust. The pressure response in wells can range from short oscillation periods in water levels (Cooper et al., 1965) to the recompilation of streamflows, which may subsequently lead to permanent changes in groundwater aquifers and wellhead responses (King et al., 1999; Montgomery & Manga, 2003).

[5] In geothermal wells in south Iceland, co- and post-seismic well level changes were observed and correlated with ground motion observations from synthetic aperture radar interferograms (Jònsson et al., 2003). Jònsson et al. (2003) found that poroelastic rebound was dominant following the earthquakes with rapid recovery of the water level. The dependency of the pore pressure on the deviatoric stress component may explain far-field water level fluctuations observed during an earthquake near Parkfield, California (Wang, 1997). While poroelastic effects also can be expected for hydraulic stimulations, these effects have not been observed/analyzed for any subsurface fluid injection projects yet. Mechanical effects (i.e., poroelastic responses in the far-field) and hydraulic effects (i.e., pressure-diffusion-related responses in the near-field) act on different timescales. Linear poroelastic theory (Biot, 1941) has been developed to predict the mechanical-driven pore pressure changes.

2 Field observations and Methods

2.1 In-situ Stimulation and Circulation (ISC) project

[6] Here, we present direct in-situ observations of these injection-induced poroelastic effects. In contrast to the aforementioned in-situ poroelastic observations related to deformation induced by large earthquakes, our study presents poroelastic deformation and pressure changes induced by fluid injection. Our study was part of the *In-situ Stimulation and Circulation* (ISC) project (Amann et al., 2018), which was carried out at the Grimsel Test Site (GTS), Switzerland, between 2015 and 2018. The experimental site was located 480 m below surface in the crystalline rock mass of the Aar Massive. The decameter-scale test volume consisted of granitic rocks and a series of brittle to ductile fault zones (Krietsch et al., 2018). The ISC rock mass was accessible through three tunnels from different sides at different elevations.

[7] The observations presented here were collected during six hydraulic fracturing experiments (Dutler et al., 2019a). The injection protocol for each experiment consisted of several cycles including (1) breakdown of the formation, (2) two to three refracturing cycles, and (3) a pressure-controlled step-test. The pressure during the injection interval reached a maximum magnitude of 21.2 MPa during the breakdown cycle (injected fluid volume < 2 L). During the subsequent fracture propagation phase, the pressure at the injection point reached values between 5.5–9.0 MPa for flow rates up to 90 L/min. In total, volumes of approximately 1000 L per test were injected.

[8] Sixty-three packer-isolated intervals in boreholes around the injection locations (Fig. 1A) allowed us to capture the 3D fracture fluid pressure response related to six stimulation experiments. The Euclidian distance r from the midpoint of the injection point to the midpoints of the pressure monitoring interval ranged from a few meters up to 100 m. Most of the pore pressure intervals in the far-field were above the injection location, with an elevation difference of 10–40 m. After each experiment, a depressurization phase was carried out by venting the

packer intervals within the pressurized zone. Up to 12 hours were required to recover the initial pore pressure levels.

2.2 Methods

[9] The presented analysis is based on the hydraulic fracturing (Dutler et al., 2019a) and hydraulic shearing (Krietsch et al., 2020a) public datasets Dutler et al. (2019b) and Krietsch et al. (2019b). For this analysis we used pressure and strain observations. The ISC monitoring setup and the description is published (Doetsch et al., 2018b).

[10] The geological model incl. borehole logs and visualization is available (Krietsch et al., 2018a) as public dataset (Krietsch et al., 2018b). The far-field pore pressure was sampled all 60 s during the HF experiments. The Data S1 includes the location of the borehole and the borehole intervals. For this the geological model visualization was updated with the additional boreholes and intervals and can be inquired by the corresponding author.

[11] The timeseries were filtered with a lowpass second order Butterworth filter for picking. The timeseries were cut into the refrac cycles (RF1, RF2 and RF3 in Fig. S1). The highlighted section in the picking plots indicates fluid injection. The shut-in time t_s is defined as the time, when fluid injection is stopped followed by an observation phase, which ends either with a new injection cycle or the depressurization of the system, opening the ISC injection and pore pressure observation intervals. The characteristic time t_c is the difference between the picking time t_{pick} and shut-in time t_s. For the pore pressure and strain observations, the time was picked due to reaching a minimum, maximum or a notable change in magnitude during the observation phase (Fig. S1). For the pore pressure timeseries we used in general the latter pick with bigger absolute magnitude, which is hydraulically driven. For the uniaxial strain timeseries, the earliest pick was used as it is an indication of mechanical driven one. All results can be found in Data S2 (pore pressure), Data S4 (strain).

[12] For each HF experiment the absolute maximum magnitudes were picked from the pore pressure timeseries during the two refrac cycles RF1 and RF2. These two cycles correspond to the biggest fluid volume without depressurization and highest flow rates. The corresponding injected volume was calculated for the time corresponding to the absolute maximum magnitude. Both results can be found in Data S3 and both are visualized (see Fig. 2B, S4A and S5B).

[13] Outside of the pressurized zone, we assume that the change in pore pressure is linked with the mean stress change $\sigma_m = \frac{1}{3}(\Delta\sigma_{11} + \Delta\sigma_{22} + \Delta\sigma_{33})$ and the Biot-Willis coefficient α. Volumetric strain is then calculated from the mean stress change and the known Young's modulus K for the rock mass. Then,

$$\Delta p = \alpha\sigma_m$$

$$\sigma_m = K\epsilon_{vol}$$

where α is between 0.64 and 0.71 and K = 19 GPa (Selvadurai, Selvadurai & Nejati, 2019).

[14] Extract from Detournay & Cheng (1988) presenting the pore-pressure solution induced by the pressurization of an infinite vertical cylinder. The three fundamental modes to solve the problem are (i) the far-field isotropic stress, (ii) the in-situ pore pressure and (iii) the far-field stress deviator.

- Mode 1

The mode 1 corresponds to the classical Lamé solution and does not include a pore pressure term.

- Mode 2

The pore pressure field is solved for an uncoupled homogeneous diffusion equation taking the Laplace transform (with inversion parameter s). For the boundary conditions in the far-field the in-situ pore pressure, p_0, is reached and the stress component vanish. The pore pressure field is solved using by the Laplace transformed solution (Eq. 23, Detournay & Cheng, 1988):

$$\frac{s\tilde{p}^{(2)}}{p_0} = -\frac{K_0(\xi)}{K_0(\beta)}$$

where K_0 is the modified Bessel function of second kind of order zero, $\xi = r\sqrt{s/D}$ and $\beta = a\sqrt{s/D}$. The parameters a and D are cylinder radius, and the diffusivity coefficient. The radius r indicates the distance between the cylinder radius and a given observation point.

- Mode 3

For a deviatoric stress field the pore pressure solution is also given in the Laplace transform domain. The solution reads:

$$\frac{s\tilde{p}^{(3)}}{S_0 \cos 2\theta} = \frac{B^2(1-\nu)(1+\nu_u)^2}{9(1-\nu_u)(\nu_u-\nu)} C_1 K_2(\xi) + \frac{B(1+\nu_u)}{3(1-\nu_u)} C_2 \frac{a^2}{r^2}$$

$$C_1 = -\frac{12\beta(1-\nu_u)(\nu_u-\nu)}{B(1+\nu_u)(D_2-D_1)}$$

$$C_2 = \frac{4(1-\nu_u)D_2}{D_2-D_1}$$

$$D_1 = 2(\nu_u-\nu)K_1(\beta)$$

$$D_2 = \beta(1-\nu)K_2(\beta)$$

where K_n is the modified Bessel function of second kind of order n. The parameters, S_0, B, ν_u, ν are stress deviator, Skempton coefficient, undrained and drained Poisson's ratio. The $\cos 2\theta$ on the lhs indicate that the problem is not axisymmetric. The first term on the rhs depends only on the modified Bessel function of order 2 all the other parameters are constant. The second term on the rhs depends on r^{-2} and is the mechanical component, which drives the magnitude

decay in the far-field. The instantaneous drilling of the cylinder generates the following approximation for the undrained pore pressure distribution given by Eq. 50 (Detournay & Cheng, 1988):

$$p^0 = \frac{4}{3} S_0 B (1 + \nu_u) \frac{{a_c}^2}{r^2} \cos 2\theta$$

[15] In the following we describe the fitting process, to achieve the "poroelastic solution" presented in Fig. 2B, S4A and S5B. Two fitting parameters are introduced with a corresponding cylinder radius, a_c and a corresponding injection time, td. The parameters for the pore pressure solution can be found in Table 1.

[16] The late time approximation $p(r, \theta)$ and p^0 are equated, where the values p_a and a for the envelope $p(r, \theta)$ are given. The two terms equated and solved for a_c to achieve the new corresponding cylinder radius. The mean stress p_0 is estimated from the six injection experiments during the refracturing cycles and the deviatoric component S_0 is the difference of the minimum and maximum principal stress magnitude divided by 2. The diffusivity coefficient is estimated from the pressurized near-field zone presented in Fig. 2A. The other values are from the literature or calculated from the values given in Table 1.

[17] The first fitting parameter gives a value a_c equal to 2.80 m allow us to match the elastic approximation with the far-field observations decaying with a rate r^{-2}. Nevertheless, we use a value of 2.60 m for pore pressure solution obtained by the numerical Laplace inversion model, due to inaccuracies due to the transformation. The numerical results in the time domain are obtained using a numerical Laplace inversion model of Stehfest (1970).

[18] Fig. S3A and S3B present the solutions for Mode 2 and Mode 3 for various times td, which corresponds to possible injection times. The pore pressure solution is then presented by the superposition of $p^{(2)} + p^{(3)}$ in Fig. S3C. The injection time in our case is around 1200 s. Indeed, the solution for td equal to 1200 s is able to build an envelope to the observations, which is a good match between the model and our observations.

The Skempton coefficient is given by (Wang, 2000):

$$B = \frac{3(\nu_u - \nu)}{\alpha(1 - 2\nu)(1 + \nu_u)}$$

3 Spatial and time effect on pore pressure response

[19] Examples of pressure data are presented in Fig. 1B. All of the pressure records were classified based on their pressure response during the experiments as being positive (pressure increase), negative (pressure decrease), or mixed (pressure increase and decrease from one experiment to the next). In addition, for each monitoring point, the perturbation magnitude was extracted. The perturbation magnitude is defined as the extremum (negative or positive) pressure perturbation magnitude observed during each experiment. The characteristic time was estimated by the elapsed time between the maximum pressure in the injection interval (which is normally the shut-in time) and pressure perturbation extremum in the observation intervals (Fig. S1).

[20] In total, we observed 28 positive, 28 negatives, and 7 mixed responses (Fig. 1C). Far-field monitoring intervals tended to always present the same response, while mixed responses were more common in the near-field. In the near-field (up to 30 m), the pressure

response was dominantly positive (Fig. 1A), although mixed and negative responses also were present.

[21] Negative pore pressure responses due to the stress/strain redistribution were driven by the fluid injection into the fractured rock mass. Positive responses were primarily associated with a hydraulic connection to the injection point, and these also may have been related to fracture closure and volumetric compression. The near-field zone dominated by positive and mixed responses is referred to as the pressurized zone. An example of a mixed response is given by the PRP11 interval presented in Fig. 1B, which showed a positive response (HF1–HF5, red) except during HF6 when a negative response was observed (blue in Fig. 1B). These exceptions were induced by local heterogeneities in the structure and flow, and such data can be explained only when the small-scale heterogeneities and their configuration with respect to the injection point are considered (Dutler et al., 2021).

[22] The pore pressure intervals in the far-field were consistently negative or positive for all experiments, i.e., there were no mixed responses, except for during experiment HF5. This can be explained by the peculiar flow situation during this test because a short-cut was created to an open borehole during the first refracturing cycle and the far-field pressure perturbation during this test was below our detection threshold. The spatial repartition of positive and negative responses was not random, and entire zones seemed to consistently present a positive or negative response.

[23] The analyses of the characteristic time showed a distinct pattern for the two zones (Fig. 2A), i.e., longer characteristic times in the near-field zone related to fluid pressure diffusion, and shorter characteristic times in the far-field zone dominated by a mechanical response. We will refer to the fracture fluid pressure for the near-field zone with a dominant fluid diffusion component. In the far-field, we will refer to the pore pressure while assuming that the fractured medium can be described equivalently with the poroelasticity.

[24] The pressurized near-field zone had diffusivity coefficients ranging from 0.01 to 1 m^2/s, as estimated by assuming normal radial diffusion in 2D, and these data are indicated by the gray dashed lines in Fig. 2A. The broad range of coefficients indicates that pressure propagation was not dominated by simple linear diffusion. Pressure propagation occurred in an interconnected fracture network with a hierarchical organization of flow from main channels initiating at the injection point and branching to subsidiary channels further away from the injection point. This geometry expanded during continuous stimulation operations (Dutler et al., 2020). Ultimately, this led to a very heterogeneous flow field with a large contrast of flow velocities as reflected by the broad range of equivalent diffusivity coefficients observed.

[25] Based on our characteristic time analyses, this near-field zone extended up to about 30 m for our experiments (Fig. 2A). This size is comparable with the extent of the pressurized zone estimated by Schopper et al. (2020) based on seismic time-lapse tomography. The zone, where we observed seismic signals, was significantly smaller with an extent of 20 m as indicated by the dashed green line of Fig. 2A (Dutler et al., 2019a; Villiger et al., 2020).

[26] In addition, 60 uniaxial strain gauges captured the strain response in this zone, and the data were indicative of complex hydromechanical interactions (Fig. S2). The strain signals exhibited very rapid responses that can be explained either by poroelastic effects or by focused flow channeling. Both processes were likely active simultaneously as supported by the

observations of some rapid pressure perturbations in the near-field that provided evidence for focused flow in deformed fractures (Fig. S5).

[27] Far-field data formed a distinct group with a faster characteristic response time leading to increased velocities. These velocities presented with equivalent diffusivity coefficients ranging from 1 to 100 m2/s (Fig. 2A). These values are unrealistically high for a diffusive process. The 1/60 Hz sampling rate used to capture the far-field pore pressure responses posed limitations for estimating the maximal diffusivity coefficient. As already discussed, the far-field responses were both positive and negative. The near-instantaneous pore pressure response in the far-field zone was suggestive of strong mechanical coupling.

[28] The analyses of the pressure perturbation magnitude (Fig. 2B) confirmed the presence of the two different processes. The pressure perturbation was largest at the injection point and in its vicinity. In the far-field, pressure perturbations were visible up to 100 m away from the injection location, although the maximum pore pressure change at that distance was only ~3 kPa. So, the ratio between the size of the pressurized zone (radius of 20–30 m) and the farthest perturbation reach was at least on the order of 3 to 5. The maximum or minimum pore pressures were generally observed during the injection phases with the highest flow rates (Fig. 1B).

[29] The largest observed pressure perturbations in the near-field up to a distance of 30 m did not exceed the pressure predicted by a radial pressure diffusion model with a diffusivity of 0.1 m^2/s, a test time of 600 s, and the actual imposed pressure at the injection point (Fig. 2B). Beyond 30 m, however, such a model predicted a pressure perturbation magnitude that was at least an order of magnitude below the largest observed perturbation. In addition, between 40 and 60 m, we mainly observed negative pressure responses, which cannot be explained by pressure diffusion.

4 Importance of static deviatoric stress field component

[30] Detournay and Cheng (1988) presented a solution for the pore pressure induced by the pressurization of a vertical cylinder with two principal stress components parallel to the cylinder axis. The cylinder axis is of infinite length. The physical interpretation of this problem can be decomposed into the following three fundamental loading modes: (i) the far-field isotropic stress, (ii) the in-situ pore pressure, and (iii) the far-field stress deviator. Each mode has to be solved, and the superposition of all three modes leads to the solution (Fig. S3). The far-field approximation (iii) of the pore pressure is asymmetric and dependent on a magnitude decay on the order of r^{-2}. A simplified approximation is presented for the volumetric pore pressure changes p:

$$p(r,\theta) = p_a \frac{a^2}{r^2} cos(2\theta),$$

where a given uniform radial stress p_a= 400 kPa and cylinder radius $a = 10$ m with the directional angle $\theta = 0$ corresponds to the upper envelope for the far-field distance in Fig. 2B. Mode (iii) has a far-field stress deviator leading to a positive and negative pore pressure response depending on the orientation, which is related to the directional angle. The zone between 30 and 50 m represents a transition zone between the pressurized zone dominated by pressure diffusion in the near-field and volumetric pore deformation in the far-field.

[31] A similar approach was used for modeling pressure around fluid disposal wells in Oklahoma, where the fluid disposal wells were located approximately 40 km away from the earthquake epicenter (Goebel et al., 2014). However, the decoupling of elasticity and diffusion has its limitations because positive and negative pore pressure responses remain unexplained. To explain the observed spectrum of pressure responses, a solution with deviatoric stress boundary conditions is required. The poroelastic solution for a cylinder given by Detournay and Cheng (1988) inherently contains this effect and can explain changes of criticality on faults in the far-field of a stimulation. The applied poroelastic solution was fitted by independent values, i.e., the corresponding cylinder radius and injection time. This allowed us to achieve a good match for the observations and the poroelastic solution presented in Fig. 2B (and Fig. S4A and S5B). Fluid flow during the experiments was limited to interconnected fractures. In the far-field zone, pressure changes were assumed to be independent of active fluid transport from the pressurized zone, which agreed well with the presented poroelastic solution.

[32] The pore pressure solution is presented for the diffusion (ii) and deviatoric (iii) components separately (Fig. 3). The diffusion component of the pore pressure solution dominated up to 42 m from the injection location. The radial pressurization was a strong simplification. Two fault zone sets S1 and S3 were striking through the targeted volume. The S3 structures were in the brittle-ductile fault zone (Fig. 3C) containing two-fracture systems (Krietsch et al., 2018). One was striking parallel to the S3 fault zone, and the other was abutting at high angles to the fault zone. The second set of ductile fault zones (S1, Fig. 3D) was associated with a single fracture system striking parallel to the fault zones. It is more likely that the injections created an ellipsoidal shaped pressurized zone along the S3 faults due to the (1) stress field, (2) fracture connectivity (3), and fracture orientation. These interconnected, permeable fractures would allow for the transportation of fluids over larger distances, but are not necessarily the most critical structures for failures depending on the stress regime. The ellipsoidal shape caused compression normal to the S3/S1 fault zones and negative pore pressure responses at the ellipsoidal tip (Fig. 3C and 3D). Compared to the deviatoric solution, which dominated the far-field response, the ellipsoid only explained the observed negative responses in front of the ellipsoidal tip occurring in front of the pressurized zone.

[33] Pore pressure responses in the far-field were the largest in magnitude for the tests (HF1, HF2, and HF6) located next to the S1 structure (Fig. 1A) and reached to only part of the magnitude for tests next to the S3 structure. The deviatoric pore pressure component (Fig. 3B) was not radially symmetric due to the deviatoric stress field component (Fig. 3E), which is given in the lower stereographic projection for the presented solution on a vertical cylinder. The six hydraulic fracturing experiments allowed us (Dutler et al., 2020; Krietsch et al., 2019a) to specify the stress state toward the direction north of the S3 structure, which is presented in the lower stereographic projection (Fig. 3E). The orientation of the minimum and maximum principal stress component was used (S_1 and S_3) for the rotation of the deviatoric component. This led to far-field pore deformation with a characteristic positive/negative response, which was dominant outside of the cylinder (Fig. 3E). The observations agreed frequently with the presented solution outside of the cylinder. A few exceptions existed around the tunnels, and these were probably influenced by secondary effects like (1) the stress field and (2) the drained rock mass.

5 Conclusions

[34] Our observations prove for the first time experimentally, that fracture fluid pressure perturbations around the injection point are not limited to the near-field, which is affected by diffusion processes. Importantly, our data show that pressure in the far-field is associated with pore volume changes. The observations indicate that an already small hydraulic power (flow rate times injection pressure) can cause a far-field poroelastic pressure response. The spatial distribution of negative and positive responses can provide important information about the dominant failure mechanism before any hazardous seismicity occurs. The spatially sparse information from the poroelastic response has the advantage that it can overcome the spatial resolution constraint of the seismic network. Thus, this can serve as a complementary method for seismic monitoring during hydraulic stimulations. With appropriate considerations, this technique could be used to develop mitigation strategies for seismic hazards, particularly if wells surrounding an injection site are equipped with packers and pressure gauges. In summary, the proposed method could represent a powerful and cost-effective monitoring tool.

Acknowledgments, Samples, and Data

Acknowledgments: This study was part of the In-situ Stimulation and Circulation (ISC) project established by the Swiss Competence Center for Energy Research-Supply of Electricity (SCCER-SoE) with the support of Innosuisse. The Grimsel Test Site is operated by Nagra, the National Cooperative for the Disposal of Radioactive Waste. We are indebted to Nagra for hosting the ISC experiment in their GTS facility and to the Nagra technical staff for on-site support and allowing us to publish the dataset of the far-field pressure response. We thank Bill Lanyon for the data compilation of the far-field pressure response.

Funding: Funding for the ISC project was provided by the ETH Foundation with grants from Shell and EWZ and by the Swiss Federal Office of Energy through a P&D grant. This research was supported by the Swiss National Foundation (Grant nos. 200021-165677 (Nathan Dutler), 200021-169178 (Hannes Krietsch)) and the Federal Institute of Technology Zurich (Grant no. ETH-35-16-1 (Linus Villiger)).

Author Contributions: The monitoring setup was designed by VG, JD, LV, HK, MRJ, and FA. The injection protocol for the HF experiments was designed by NOD and BV. All of the authors were part of the data acquisition team during the experiments of the ISC project; FA was the project administrator. The data curation, formal analysis, investigation, and data visualization, including writing the original draft, were done by NOD with the help of BV and FA. The writing, review, and editing were done by MRJ, LV, HK, VG, and JD.

Competing Interests: The authors declare no competing interests.

Data and Materials Availability: All of the material for the analysis is available in the supplementary material. The raw data are available under an open access license for non-commercial use and are accessible via the ETH research collection at https://doi.org/10.3929/ethz-b-000328270 (Dutler et al., 2019b), https://doi.org/10.3929/ethz-b-000328266 (Krietsch et al., 2019b), and https://doi.org/10.3929/ethz-b-000243199 (Krietsch et al., 2018b).

References

F. Amann, V. Gischig, K. Evans, J. Doetsch, R. Jalali, B. Valley, H. Krietsch, N. Dutler, L. Villiger, B. Brixel, M. Klepikova, A. Kittilä, C. Madonna, S. Wiemer, M. O. Saar, S. Loew, T. Driesner, H. Maurer, D. Giardini, The seismo-hydromechanical behavior during deep geothermal reservoir stimulations: open questions tackled in a decameter-scale in situ stimulation experiment. Solid Earth 9(1), 115–137 (2018). https://doi.org/10.5194/se-9-115-2018

X. Bao, D. W. Eaton, Fault activation by hydraulic fracturing in western Canada. Science 354(6318), 1406–1409 (2016). https://doi.org/10.1126/science.aag2583

P. Bhattacharya, R. C. Viesca, Fluid-induced aseismic fault slip outpaces pore-fluid migration. Science 364(6439), 464–468 (2019). https://doi.org/10.1126/science.aaw7354

M. A. Biot, General theory of three-dimensional consolidation. Journal of Applied Physics 12, 155 (1941). https://doi.org/10.1063/1.1712886

M. Calò, C. Dorbath, F. H. Cornet, N. Cuenot, Large-scale aseismic motion identified through 4-D P-wave tomography. Geophysical Journal International 186(3), 1295–1314 (2011). https://doi.org/10.1111/j.1365-246X.2011.05108.x

H. Cooper, J. Bredehoeft, I. Papadopulos, R. Bennett, The Response of Well-Aquifer Systems to Seismic Waves. Journal of Geophysical Research 70(16), 3915–3926 (1965).

M. L. T. Dambly, M. Nejati, D. Vogler, M. O. Saar, On the direct measurement of shear moduli in transversely isotropic rocks using the uniaxial compression test. Int. J. Rock Mech. Min. Sci. 113, 220–240 (2019).

E. Detournay, A. H.-D. Cheng, Poroelastic response of a borehole in a non-hydrostatic stress field. International Journal of Rock Mechanics and Mining Sciences & Geomechanics Abstracts 25(3), 171–182 (1988). https://doi.org/10.1016/0148-9062(88)92299-1

J. Doetsch, V. S. Gischig, L. Villiger, H. Krietsch, M. Nejati, F. Amann, M. Jalali, C. Madonna, H. Maurer, S. Wiemer, T. Driesner, D. Giardini, Subsurface Fluid Pressure and Rock Deformation Monitoring Using Seismic Velocity Observations. Geophysical Research Letters 45(19), 10389–10397 (2018a). https://doi.org/10.1029/2018GL079009

J. Doetsch, V. Gischig, H. Krietsch, L. Villiger, F. Amann, N. Dutler, M. Jalali, B. Brixel, C. Roques, P.L. Giertzuch, A. Kittilä, R. Hochreutener, "Grimsel ISC Experiment Description" (Tech. Rep. Zurich, 2018b). https://doi.org/10.3929/ethz-b-000310581

N. O. Dutler, B. Valley, V. Gischig, L. Villiger, H. Krietsch, J. Doetsch, B. Brixel, M. Jalali, F. Amann, Hydraulic fracture propagation in a heterogeneous stress field in a crystalline rock mass. Solid Earth 10(6), 1877–1904 (2019a). https://doi.org/10.5194/se-10-1877-2019

N. O. Dutler, V. Gischig, J. Doetsch, M. Jalali, H. Krietsch, F. Amann, Hydro mechanical data set from the six Grimsel ISC hydraulic fracturing experiments, (2019b). https://doi.org/10.3929/ethz-b-000328270

N. O. Dutler, B. Valley, V. S. Gischig, M. Jalali, B. Brixel, H. Krietsch, C. Roques, F. Amann, Hydromechanical insight of fracture opening and closure during in-situ hydraulic

fracturing in crystalline rock. Int. J. Rock Mech. Min. Sci. 135(10), 104450 (2020). https://doi.org/10.1016/j.ijrmms.2020.104450

N. O. Dutler, B. Valley, L. Villiger, V. Gischig, F. Amann, Observation of a repeated step-wise fracture growth during hydraulic fracturing experiment at the Grimsel Test Site. In Proceedings World Geothermal Conference, Reykjavik, 21–26 May 2021.

W. L. Ellsworth, Injection-Induced Earthquakes. Science 341(6142), 1225942–1225942 (2013). https://doi.org/10.1126/science.1225942

C. Frohlich, Two-year survey comparing earthquake activity and injection-well locations in the Barnett Shale, Texas. Proceedings of the National Academy of Sciences of the United States of America 109(35), 13934–13938 (2012). https://doi.org/10.1073/pnas.1207728109

T. H. W. Goebel, M. Weingarten, X. Chen, J. Haffener, E. E. Brodsky, The 2016 Mw5.1 Fairview, Oklahoma earthquakes: Evidence for long-range poroelastic triggering at >40 km from fluid disposal wells. Earth and Planetary Science Letters 472, 50–61 (2017). https://doi.org/10.1016/j.epsl.2017.05.011

T. H. W. Goebel, E. E. Brodsky, The spatial footprint of injection wells in a global compilation of induced earthquake sequences. Science 361(6405), 899–904 (2018). https://doi.org/10.1126/science.aat5449

Y. Guglielmi, F. Cappa, J.-P. Avouac, P. Henry, D. Elsworth, Seismicity triggered by fluid injection – induced aseismic slip. Science 348(6240), 1224–1227 (2015). https://doi.org/10.1126/science.aab0476

S. Jónsson, P. Segall, R. Pedersen, G. Björnsson, Post-earthquake ground movements correlated to pore-pressure transients. Nature 424(6945), 179–183 (2003). https://doi.org/10.1038/nature01776

K. M. Keranen, M. Weingarten, G. A. Abers, B. A. Bekins, S. Ge, Sharp increase in central Oklahoma seismicity since 2008 induced by massive wastewater injection. Science 345(6195), 448–451 (2014). https://doi.org/10.1126/science.1255802

C.-Y. King, S. Azuma, G. Igarashi, M. Ohno, H. Saito, H. Wakita, Earthquake-related water-level changes at 16 closely clustered wells in Tono, central Japan. Journal of Geophysical Research: Solid Earth 104(B6), 13073–13082 (1999). https://doi.org/10.1029/1999JB900080

H. Krietsch, J. Doetsch, N. Dutler, M. Jalali, V. Gischig, S. Loew, F. Amann, Comprehensive geological dataset describing a crystalline rock mass for hydraulic stimulation experiments. Scientific Data 5, 180269 (2018a). https://doi.org/10.1038/sdata.2018.269

H. Krietsch, J. Doetsch, N. Dutler, M. Jalali, V. Gischig, S. Loew, F. Amann, Comprehensive geological dataset for a fractured crystalline rock volume at the Grimsel Test Site, (2018b). https://doi.org/10.3929/ethz-b-000243199

H. Krietsch, V. Gischig, K. Evans, J. Doetsch, N. O. Dutler, B. Valley, F. Amann, Stress Measurements for an In Situ Stimulation Experiment in Crystalline Rock: Integration of Induced Seismicity, Stress Relief and Hydraulic Methods. Rock Mechanics and Rock Engineering 52(2), 517–542 (2019a). https://doi.org/10.1007/s00603-018-1597-8

H. Krietsch, V. Gischig, J. Doetsch, M. Jalali, F. Amann, Hydro mechanical data set from the six Grimsel ISC hydraulic shearing experiments, (2019b). https://doi.org/10.3929/ethz-b-000328266

H. Krietsch, V. S. Gischig, J. Doetsch, K. F. Evans, L. Villiger, M. Jalali, B. Valley, S. Loew, F. Amann, Hydro-mechanical processes and their influence on the stimulation effected volume: Observations from a decameter-scale hydraulic stimulation project. Solid Earth Discuss., (2020). https://doi.org/10.5194/se-2019-204

D. R. Montgomery, M. Manga, Streamflow and water well responses to earthquakes. Science 300(5628), 2047–2049 (2003). https://doi.org/10.1126/science.1082980

F. Schopper, J. Doetsch, L. Villiger, H. Krietsch, V. S. Gischig, M. Jalali, F. Amann, N. Dutler, H. Maurer, On the Variability of Pressure Propagation during Hydraulic Stimulation based on Seismic Velocity Observations. Journal of Geophysical Research: Solid Earth 125, e2019JB018801 (2020). https://doi.org/10.1029/2019JB018801

P. Selvadurai, P. A. Selvadurai, M. Nejati, A multi-phasic approach for estimating the Biot coefficient for Grimsel granite. Solid Earth 10, 2001–2014 (2019).

H. Stehfest, Algorithm 368: Numerical inversion of Laplace transforms [D5]. Commun. ACM 13, (1970). doi:10.1145/361953.361969

L. Villiger, V. S. Gischig, J. Doetsch, H. Krietsch, N. O. Dutler, M. Jalali, B. Valley, P. A. Selvadurai, A. Mignan, K. Plenkers, D. Giardini, F. Amann, S. Wiemer, Influence of reservoir geology on seismic response during decameter-scale hydraulic stimulations in crystalline rock. Solid Earth 11(2), 627–655 (2020). https://doi.org/10.5194/se-11-627-2020

H. F. Wang, Effects of deviatoric stress on undrained pore pressure response to fault slip. Journal of Geophysical Research 102(97), 17943–17950 (1997).

H. Wang, Theory of Linear Poroelasticity with Applications to Geomechanics and Hydrogeology (Princeton University Press, 2000).

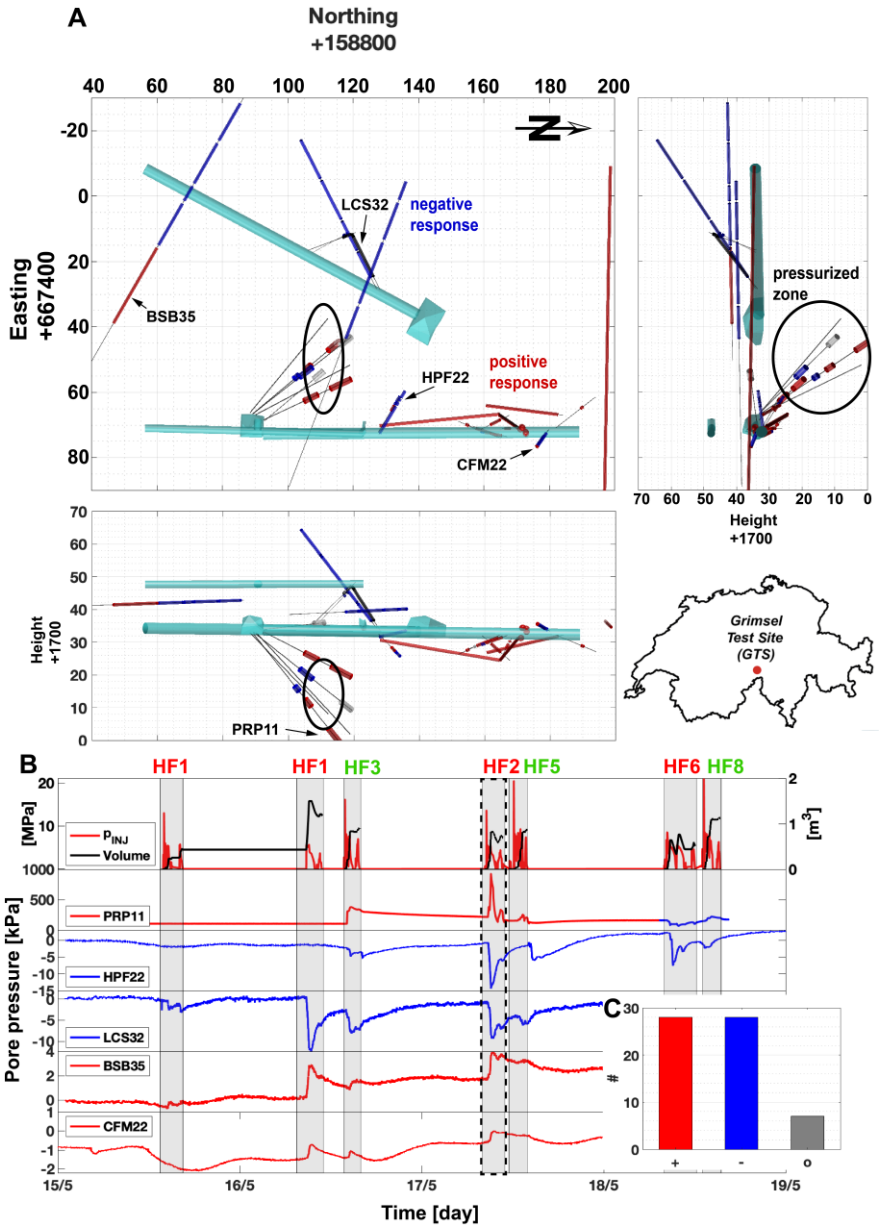

Fig. 1. Time series of the pore pressure observations were classified by positive or negative responses. (**A**) The interval locations are indicated and labeled in the plane and profile view, and data show the positive (red), negative (blue), and mixed (gray) magnitude response in the open intervals including the approximate pressurized zone and access tunnels. Coordinates on panel (**A**) are referenced to the Swiss metric coordinate system (CH1903+). (**B**) Time series of the injection pressure (red solid) and volume (black solid), where PRP11 is the open interval pressure in the pressurized zone and the other four are open intervals indicative of the far-field response. The location of the intervals is indicated in (**A**). (**C**) Proportion of positive, negative, and mixed responses.

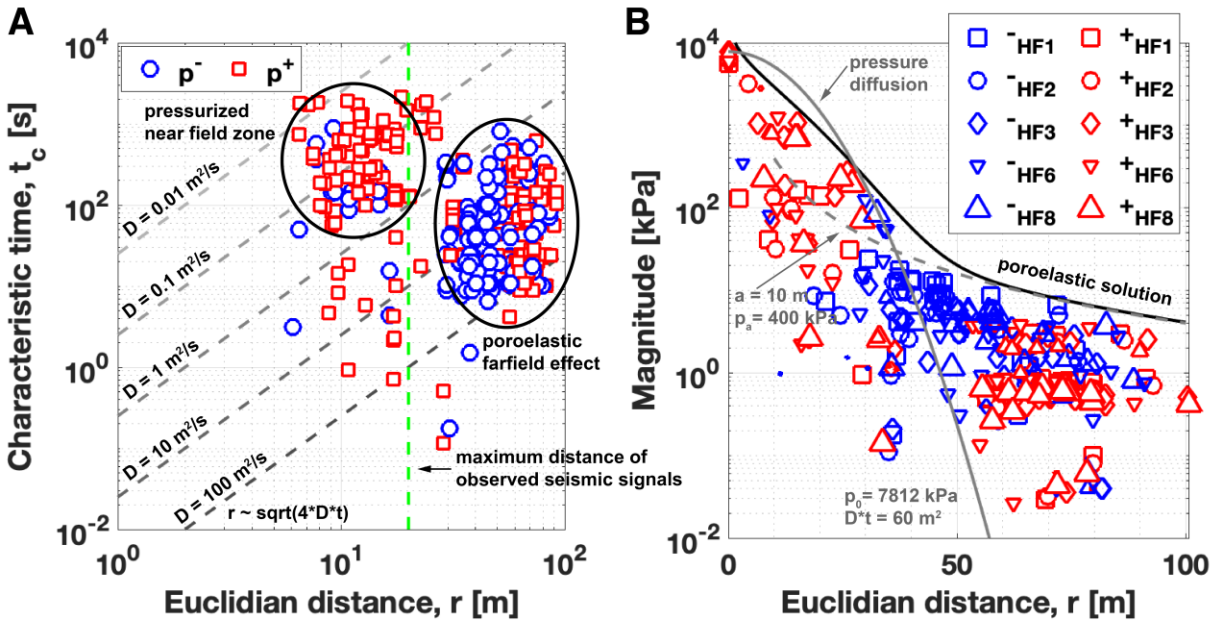

Fig. 2. Spatial time increase and spatial maximum absolute pressure magnitude were classified as positive (red) and negative (blue). (**A**) The log–log plot presents the characteristic time t_c against the Euclidian distance r along with gray dashed lines that indicate the different diffusivity coefficients for the 1D diffusion equation. Two different patches were observed for the pressure observations, one corresponding to the pressurized near-field zone and the other to the poroelastic far-field response. The green dashed line indicates the maximum distance of observed seismic signals. (**B**) The maximum magnitude is presented, including the volume dependent size of the symbols against the Euclidian distance r for specific tests on a semi-log scale (see Fig. S4A for the log–log scale). The poroelastic solution (black solid line), radial pressure diffusion (gray solid line), and far-field pore pressure solution are drawn (gray dashed line).

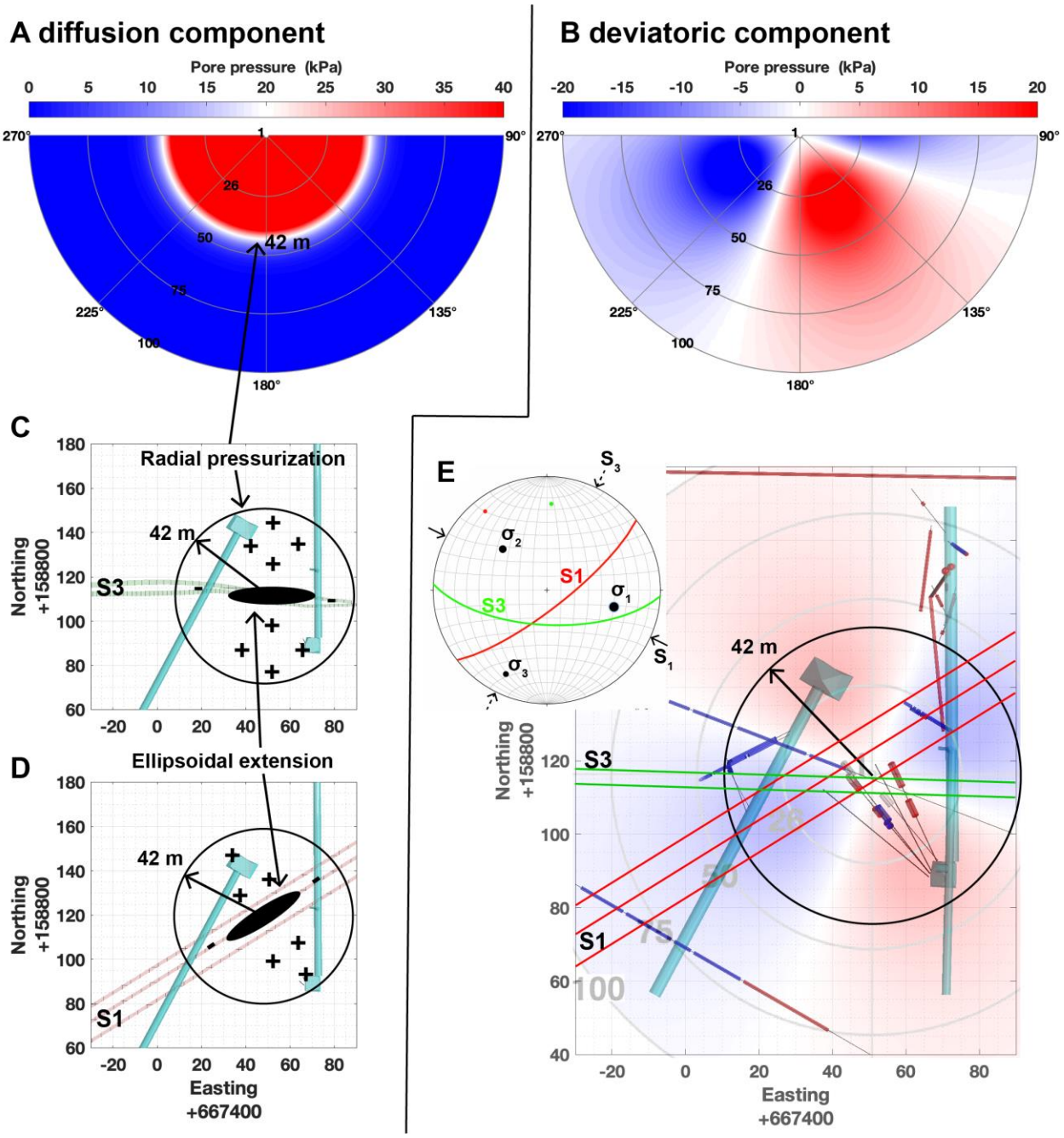

Fig. 3. Pore pressure response as interpreted by the diffusion and deviatoric component. (**A**) The pressurized radial-symmetric solution for a cylinder dominated up to 42 m with a magnitude of 20 kPa. (**B**) The deviatoric component started to dominate after 42 m (solid circle in **C**–**E**). Depending on the injection location (**C**) next to the structure S3 or (**D**) S1, the near field was more likely along the natural, pre-existing fractures, and it formed an ellipsoidal extension. (**E**) The pore pressure observations outside of the cylinder agreed often with the deviatoric component. Even in the cylinder, negative pore pressure was observed due to the deviatoric stress field and undrained dominant fault response, which acted in concert.

520
521

522 **Table 1.** Parameters of the poroelastic model used for the poroelastic solution.

Quantity	Value	Unit
$\boldsymbol{p_0}$	7812	[kPa] *(this study)*
$\boldsymbol{S_0}$	4000	[kPa] (Dutler et al., 2020)
$\boldsymbol{\nu}$	0.2	[] (Dambly et al., 2019)
$\boldsymbol{\nu_u}$	0.33	[] (Wang, 2000)
$\boldsymbol{\alpha}$	0.68	[] (Selvadurai, Selvaduray & Nejati, 2019)
$\boldsymbol{D}$	0.1	$[m^2/s]$ *(this study)*
$\boldsymbol{B}$	0.719	[] *(this study)*
$\boldsymbol{K}$	19	[GPa] (Dambly et al., 2019)
$\boldsymbol{G}$	10	[GPa] (Dambly et al., 2019)

523
524